International Journal of Power Electronics and Drive System (IJPEDS)
Vol. 17, No. 4, December 2026, pp. 2457~2473
ISSN: 2088-8694, DOI: 10.11591/ijpeds.v17.i4.pp2457-2473

Implementation of hysteresis current control for BLDC motor utilization TI DSP LaunchPad F28379D

Amir Haziq Nordin[1], Auzani Jidin[1], Azrita Alias[1], Tole Sutikno[2]
[1]Faculty of Electrical Technology and Engineering, Universiti Teknikal Malaysia Melaka, Melaka, Malaysia
[2]Department of Electrical Engineering, Faculty of Industrial Technology, Universitas Ahmad Dahlan, Yogyakarta, Indonesia

Article Info

Article history:

Received Jul 9, 2026
Revised Aug 26, 2026
Accepted Oct 4, 2026

Keywords:

Basic switching commutation
BLDC motor
Current ripple
Hysteresis current control
Motor drive
Real-time control
TI DSP F28379D

ABSTRACT

Brushless direct current (BLDC) motors are employed in a broad range of industrial and automotive systems because of their high efficiency and favorable torque density. However, conventional basic switching commutation (BSC) often results in high current ripple during commutation. This paper presents the implementation of hysteresis current control (HCC) for a three-phase BLDC motor using the Texas Instruments Digital Signal Processor (DSP) LaunchPad F28379D. A complete simulation model is developed in MATLAB/Simulink, followed by hardware validation. The performance of HCC is compared with BSC in terms of current ripple under different hysteresis bandwidths and PWM frequencies. Experimental results show that HCC significantly reduces current ripple while maintaining good dynamic response. The study confirms that HCC integrated with the TI DSP platform offers improved current regulation suitable for precision motor drive applications.

This is an open access article under the CC BY-SA license.

Corresponding Author:

Auzani Jidin
Fakulti Teknologi dan Kejuruteraan Elektrik, Universiti Teknikal Malaysia Melaka
76100 Hang Tuah Jaya, Melaka, Malaysia
Email: auzani@utem.edu.my

1. INTRODUCTION

Brushless direct current (BLDC) machines are used across industrial automation, automotive systems, robotics, and consumer products. Their adoption is supported by characteristics such as high efficiency, a favorable torque-to-weight ratio, compact construction, rapid dynamic response, and reduced maintenance requirements relative to brushed DC machines [1], [2]. Their superior torque-to-weight ratio and high reliability make them particularly suitable for applications in electric vehicles, unmanned vehicles, heating, ventilation, and air conditioning (HVAC) systems, as well as precision motion control [3]. As these applications demand high efficiency and precise torque regulation, the development of effective current control strategies for BLDC motor drives has become increasingly important.

Conventional basic switching commutation (BSC) is widely employed in BLDC motor drives because of its simple implementation and low computational complexity. However, BSC operates without closed-loop current regulation, resulting in significant current ripple during commutation. Excessive current ripple produces undesirable torque pulsations, audible noise, mechanical vibration, and reduced drive efficiency, particularly in applications requiring smooth torque production and accurate current regulation [4]–[6]. Therefore, an effective current control strategy is required to improve the dynamic performance and current quality of BLDC motor drives.

Several advanced control techniques have been proposed to address these limitations. Field-oriented control (FOC) and direct torque control (DTC) are capable of providing excellent dynamic performance and

accurate torque regulation [4], [7]. Nevertheless, these methods require accurate motor parameters, coordinate transformations, rotor position estimation, and relatively high computational resources, making their implementation more complex for practical embedded systems [8]. In contrast, hysteresis current control (HCC) offers a simple nonlinear current control strategy with inherent current limiting, fast transient response, and excellent current tracking capability by maintaining the phase current within a predefined hysteresis band [9], [10]. Owing to its simplicity and robustness, HCC has attracted considerable attention for high-performance motor drive applications.

Despite these advantages, existing studies on HCC-based BLDC motor drives mainly focus on controller design or simulation-based validation, while comparatively less attention has been given to complete real-time implementation using high-performance digital signal processor (DSP) platforms [11]. Furthermore, practical implementation aspects, including Hall-sensor decoding, current sensor calibration, and seamless integration between MATLAB/Simulink and embedded DSP hardware, are often only briefly discussed.

In response to these implementation considerations, this paper develops and experimentally evaluates an HCC scheme for a three-phase BLDC motor controlled by the Texas Instruments TMS320F28379D DSP LaunchPad. The proposed controller was first developed in MATLAB/Simulink and subsequently deployed to the DSP for real-time experimental validation. In addition to implementing the HCC algorithm, this work integrates Hall-sensor decoder logic, current sensor zero-offset calibration, and real-time current regulation into a complete BLDC motor drive system. The effects of hysteresis bandwidth and PWM switching frequency on current ripple are then systematically investigated through simulation and hardware experiments. The experimental results demonstrate that the proposed implementation significantly improves current regulation compared with conventional basic switching commutation (BSC), providing practical design guidance for DSP-based BLDC motor drive applications.

The principal contributions of this work are summarized as follows: i) Development and real-time implementation of a hysteresis current controller on the TI TMS320F28379D DSP platform using MATLAB/Simulink; ii) Integration of Hall-sensor decoding, current sensing, and zero-offset calibration into a complete BLDC motor drive implementation; iii) Systematic investigation of the effects of hysteresis bandwidth and PWM switching frequency on current ripple through simulation and experimental validation; and iv) Experimental comparison between the proposed HCC implementation and conventional basic switching commutation (BSC) to demonstrate the effectiveness of the proposed controller.

2. METHOD

Two commutation strategies for a three-phase BLDC motor are considered: BSC and HCC. BSC is an open-loop method that sequences the inverter switches solely from Hall sensor signals (Ha, Hb, Hc). HCC adds a closed-loop current regulator that forces each phase current to remain within a programmable hysteresis band, delivering smooth torque and reduced ripple [9], [12].

The total electromagnetic torque produced by a BLDC motor is the sum of the torques from each phase [13]:

$$T_{e,total} = T_{e,a} + T_{e,b} + T_{e,c} = k_{t,a}i_a + k_{t,b}i_b + k_{t,c}i_c \quad (1)$$

where $k_{t,a}, k_{t,b}, k_{t,c}$ are the torque constants and i_a, i_b, i_c are the phase currents [13]. Thus, precise torque control requires precise current regulation [14]. Figure 1 illustrates two fundamental concepts: (a) the six non-zero voltage space vectors for two-phase conduction, each corresponding to one switching state, and (b) the production of torque over time, showing that positive current yields positive torque, zero current yields zero torque, and negative current yields negative torque. Any deviation from the ideal current waveform directly translates into torque ripple, highlighting the need for precise current regulation [15], [16].

The flowchart in Figure 2 explains how the Hall sensor signals (Ha, Hb, Hc) are decoded to determine which phase pair should be active and which torque constant applies, as illustrated in Figure 1(b). This decision directly implements (1) by selecting the appropriate current path, thereby linking the Hall state to the instantaneous torque contribution from each phase. As shown in Figure 3, the torque hysteresis controller (THC) uses a two-level comparator for each controlled phase. Each comparator evaluates its corresponding phase-current error, and its output determines the voltage vector applied by the inverter so that the current is regulated relative to the specified hysteresis limits.

This experiment implements HCC digitally on a TMS320F28379D DSP and compares its performance against BSC in terms of current ripple, torque smoothness, and response to changes in hysteresis bandwidth and PWM frequency. The following subsections detail the decoder logic, current sensing, DSP implementation, and experimental hardware.

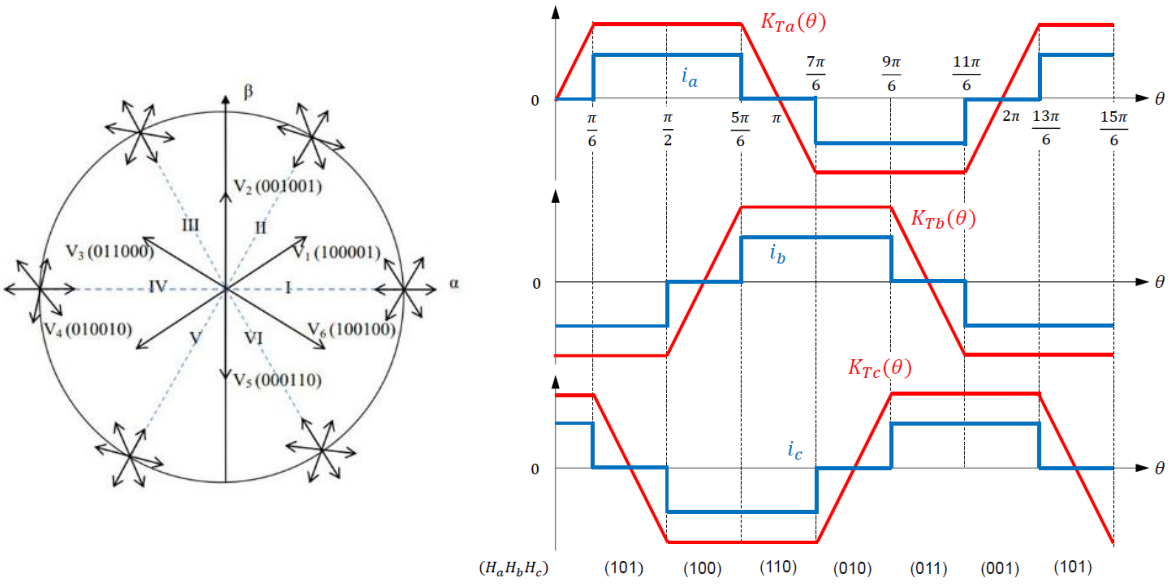

(a) (b)

Figure 1. (a) Representation of two-phase voltage space vectors and (b) production of torque in a BLDC motor

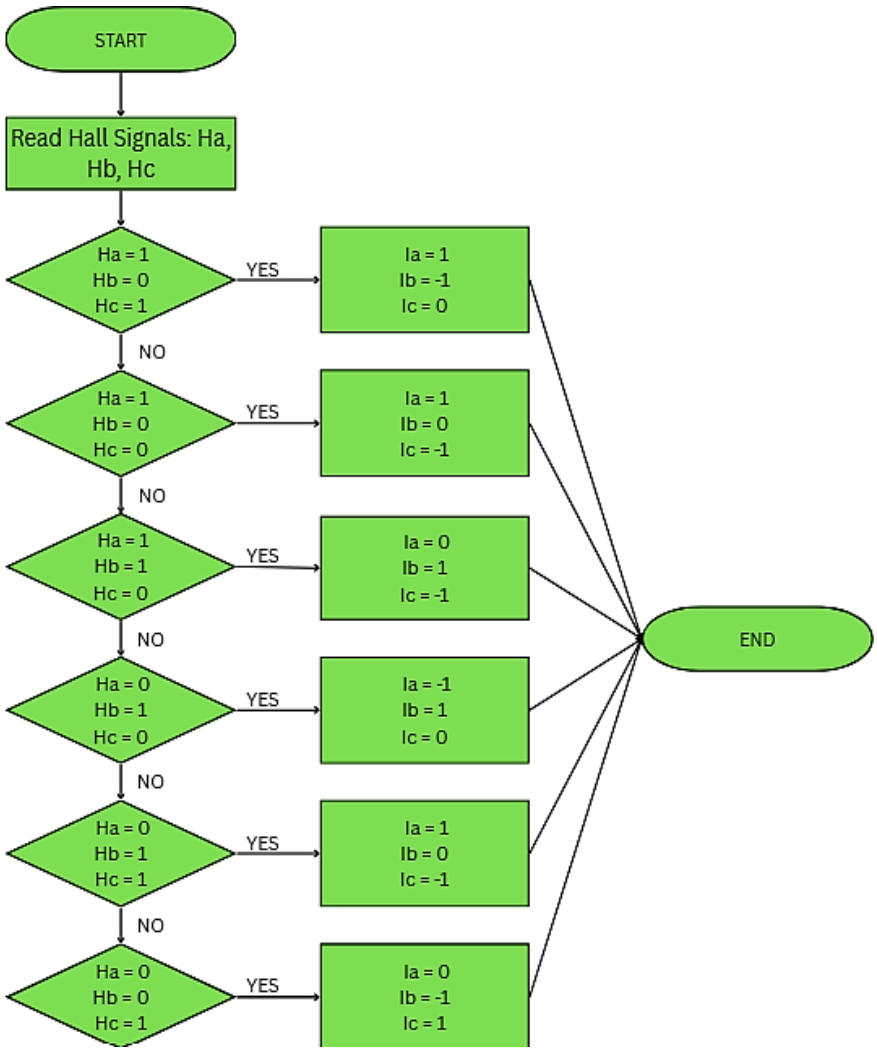

Figure 2. Flowchart for Hall sensor decoding to active phases with torque constants and currents

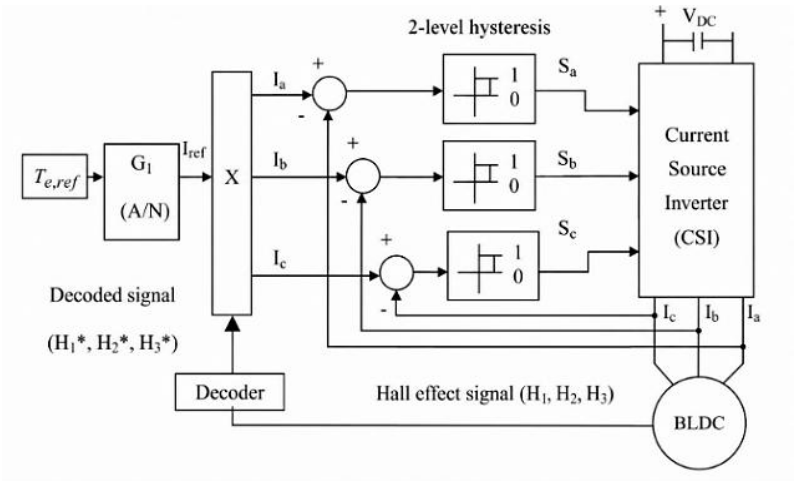

Figure 3. Block diagram for BLDC motor drive with hysteresis current control

2.1. Decoder logic and commutation

Six-step commutation requires, two motor phases conduct at a time, with the third floating [17]. The active phase pair and current direction are determined by the three Hall sensor signals (Ha, Hb, Hc). The Boolean expressions for the inverter switches are derived in Figure 4. During operation, the Hall sensors provide rotor-position information to the DSP, which uses the decoded state to determine the commutation sequence. A reference current is assigned to each conducting phase, while the corresponding measured current is obtained from the current-sensing circuit. The controller evaluates the difference between these two signals. If the measured current error passes the upper hysteresis threshold, the relevant inverter switch is turned OFF to reduce the current. If the error falls below the lower threshold, the switch is turned ON to raise the current. These decisions are repeated during operation to regulate the phase current within the selected band while maintaining the required electronic commutation sequence.

$$S1 = \bar{H_b} \cdot H_c, \quad S2 = H_b \cdot \bar{H_c}, \quad S3 = H_a \cdot \bar{H_c},$$
$$S4 = \bar{H_a} \cdot H_c, \quad S5 = \bar{H_a} \cdot H_b, \quad S6 = H_a \cdot \bar{H_b}$$

Figure 4. Boolean expression of BSC method

2.2. Hysteresis current control strategy

HCC is a nonlinear feedback method that maintains each phase current of a BLDC motor within a predefined tolerance band around reference current [12], [18]. Figure 5(a) shows the block diagram. For each active phase, the current error is defined as in (2) [13].

$$e = i_{\text{ref}} - i_{\text{meas}} \tag{2}$$

A hysteresis comparator with an upper bound $(+\text{HB})$ and a lower bound $(-\text{HB})$ processes this error. When $e > +\text{HB}$, the controller applies a voltage vector that decreases the current. When $e < -\text{HB}$, it applies a vector that increases the current. This relay control forces the actual current to oscillate within the hysteresis band, as depicted in Figure 5(b), which illustrates the resulting current oscillation within the hysteresis band and the corresponding switching signal (S_x). The measured current (i_{meas}) alternately rises and falls, crossing the reference (i_{ref}), while the switching signal turns on and off accordingly. Because the electromagnetic torque of a BLDC motor is proportional to the current phase, precise current regulation yields smooth torque with reduced ripple. The reference current (i_{ref}) is a square waveform synchronized with the Hall decoder states in Table 1, and its amplitude is set by the desired torque.

2.3. Simulation model of HCC and BSC of BLDC motor

Figures 6 and 7 illustrate the simulation models of the BLDC motor drive system developed to evaluate the performance of the proposed hysteresis current control (HCC) and basic switching commutation

(BSC) strategies. Figure 6 represents the closed-loop HCC configuration, in which the measured phase currents are compared with their respective reference currents to generate current error signals. These error signals are processed by the hysteresis controller to determine the appropriate switching states of the inverter, allowing the phase currents to be regulated within the specified hysteresis band. In contrast, Figure 7 presents the open-loop BSC configuration, where the switching sequence is determined based on the Hall sensor signals without employing a closed-loop phase current regulation mechanism. Both simulation models operate under the same applied speed reference to ensure a consistent basis for comparison. The simulation results are subsequently used to evaluate the differences in phase current behaviour and electromagnetic torque response between the two control strategies.

The core subsystem is the BLDC motor subsystem, which models the motor's electrical and mechanical behaviour. It takes three-phase inputs (Sa, Sb, Sc), a mechanical load (TL), and Hall signals to simulate speed, torque, and current response. The input Tref block represents the reference torque for the motor. This is sent to a conventional control method. Each reference phase is compared using sum or subtract blocks to generate error signals, which feed into the switching control logic (likely generating the Sa, Sb, Sc signals). These in turn control the motor phases. The Hall sensor inputs are also fed into the BLDC subsystem to provide position feedback.

The control section consists of the counterclockwise (CCW) logic control block, which is responsible for generating the appropriate inverter switching sequence based on the rotor position information obtained from the three Hall sensors (H1, H2, and H3). These Hall sensor signals represent the instantaneous rotor position and are processed through a predefined Boolean logic system to determine the appropriate commutation state. Based on the detected Hall sensor combination, the CCW logic block generates six switching signals (S1–S6), which determine the ON and OFF states of the corresponding insulated-gate bipolar transistors (IGBTs) in the three-phase voltage source inverter. During six-step commutation, two motor phases are energized simultaneously, while the third phase remains in a floating state, allowing current to flow through the selected phase pair and generate electromagnetic torque. The switching sequence is continuously updated according to the Hall sensor signals to ensure proper phase commutation and maintain motor rotation in the counterclockwise direction. Consequently, the CCW logic block plays an essential role in synchronizing the inverter switching operation with the rotor position to achieve continuous motor rotation.

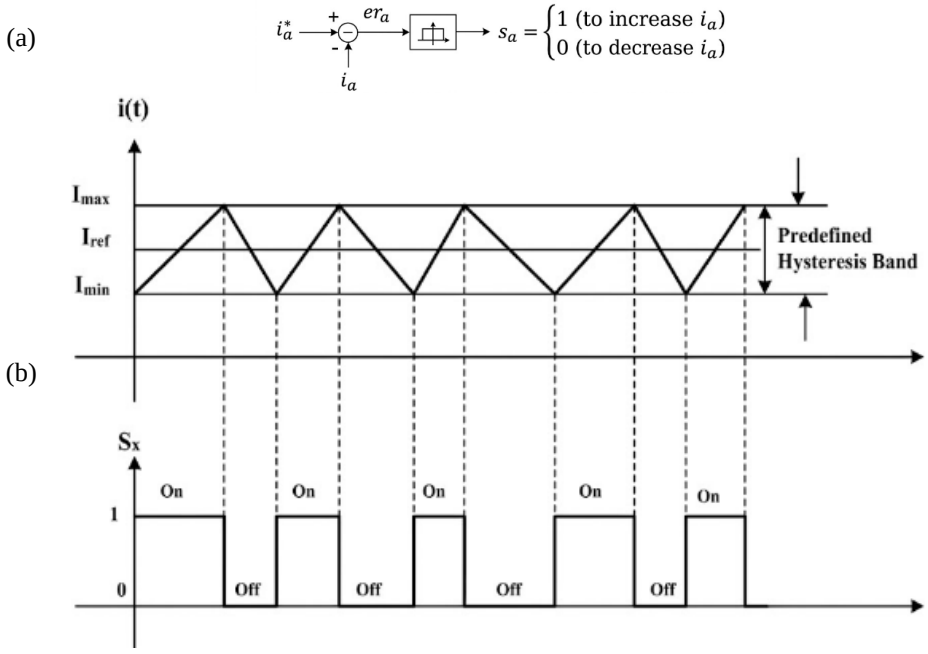

Figure 5. Hysteresis current control: (a) block diagram; (b) current waveform with the corresponding switching signal

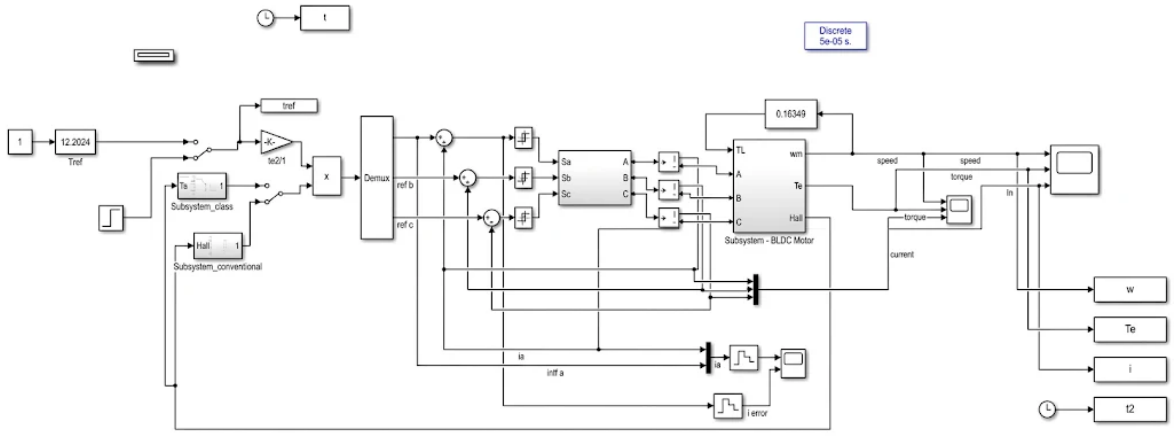

Figure 6. Simulation model THC of BLDC motor drive

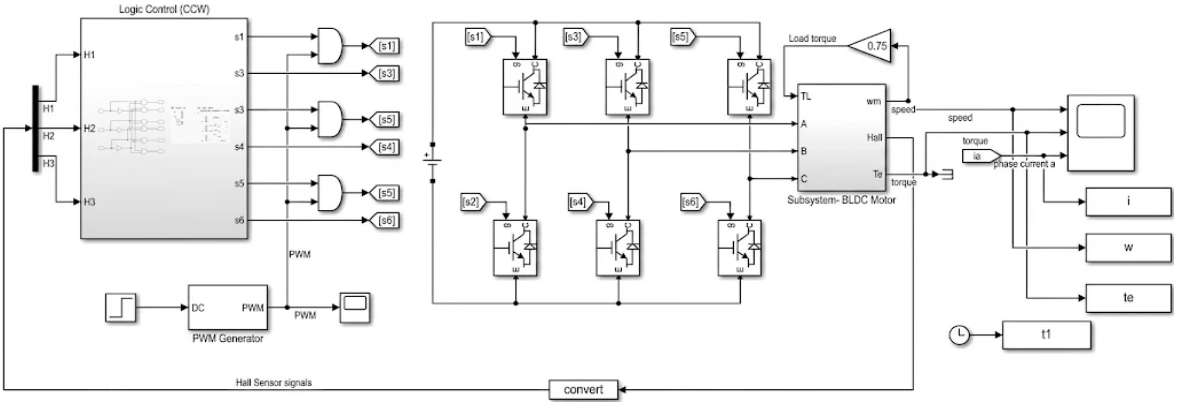

Figure 7. Simulation model BSC of BLDC motor drive

2.3.1. Implementation of decoder circuit

The decoder ensures that at any instant, only two switches (one high-side and one low-side from different phases) are closed, while the third phase floats [19]. Figure 8(a) shows the decoder circuit waveform for BSC, while Figure 8(b) shows the corresponding waveform for HCC. The switching patterns appear similar, but the presence of current feedback in HCC modifies the current phase and flux alignment, leading to smoother torque production [17], [20]. Tables 1 and 2 present the truth tables for the BSC and HCC methods, respectively, showing the relationship between Hall sensor signals, IGBT switching states, and phase current directions. Both methods use six-step commutation, in which two phases conduct simultaneously while the third phase remains inactive. However, HCC incorporates current feedback to regulate the phase currents according to the hysteresis control strategy. Table 3 further compares the phase current and flux conditions of both methods at 1.2 s and 1.3 s, highlighting the differences in phase behaviour between BSC and HCC. These comparisons demonstrate how current feedback influences phase current regulation and contributes to improved current control performance.

Table 1. Truth table for BSC method

Hall sensor signal			Switching state for IGBT						Current phase		
Ha	Hb	Hc	S1	S2	S3	S4	S5	S6	Ia	Ib	Ic
0	0	1	1	0	0	1	0	0	+1	-1	0
1	0	1	0	1	1	0	0	0	-1	+1	0
1	0	0	0	0	0	1	0	1	0	+1	-1
1	1	0	0	0	0	1	1	0	0	-1	+1
0	1	0	0	0	0	1	0	1	-1	0	+1
0	1	1	1	0	0	0	0	1	+1	0	-1

Table 2. Truth table for the HCC method

Hall sensor signal			Switching State for IGBT						Current phase		
Ha	Hb	Hc	S1	S2	S3	S4	S5	S6	Ia	Ib	Ic
0	0	1	1	0	0	0	1	0	+1	-1	0
1	0	1	0	1	1	0	0	0	-1	+1	0
1	0	0	0	0	0	1	0	1	0	+1	-1
1	1	0	0	0	0	1	1	0	0	-1	+1
0	1	0	0	0	0	1	0	1	-1	0	+1
0	1	1	1	0	0	0	0	1	+1	0	-1

Table 3. Analysis of BSC and HCC waveform

Parameter		Analysis of BSC waveform			Analysis of HCC waveform		
	Time (s)	Phase A	Phase B	Phase C	Phase A	Phase B	Phase C
Current	1.2	Positive	Negative	Zero	Positive	Negative	Zero
	1.3	Positive	Zero	Negative	Negative	Positive	Zero
Flux	1.2	Zero	Negative	Positive	Positive	Negative	Zero
	1.3	Positive	Negative	Zero	Negative	Positive	Zero

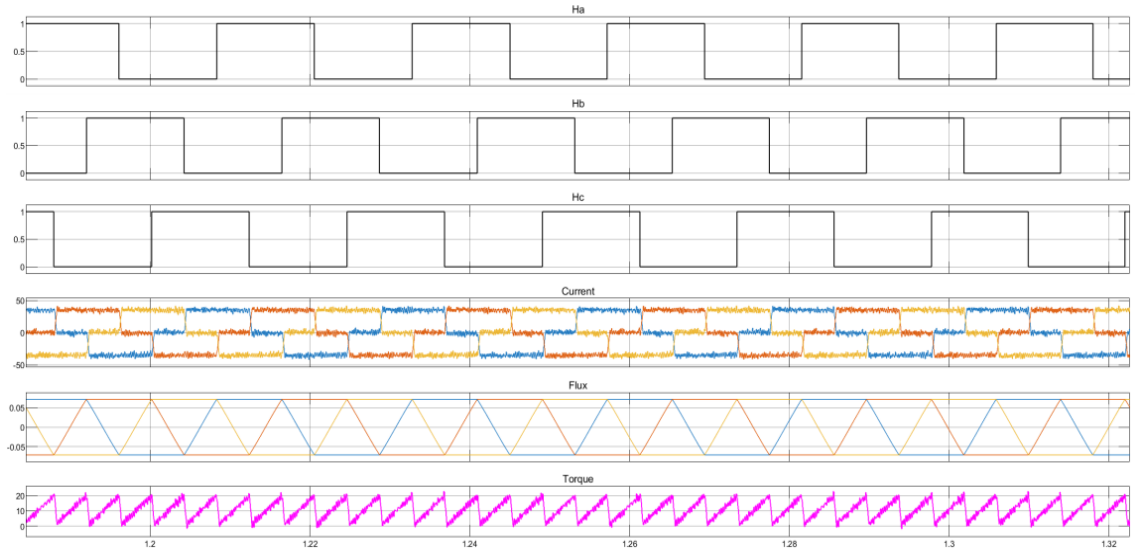

(a)

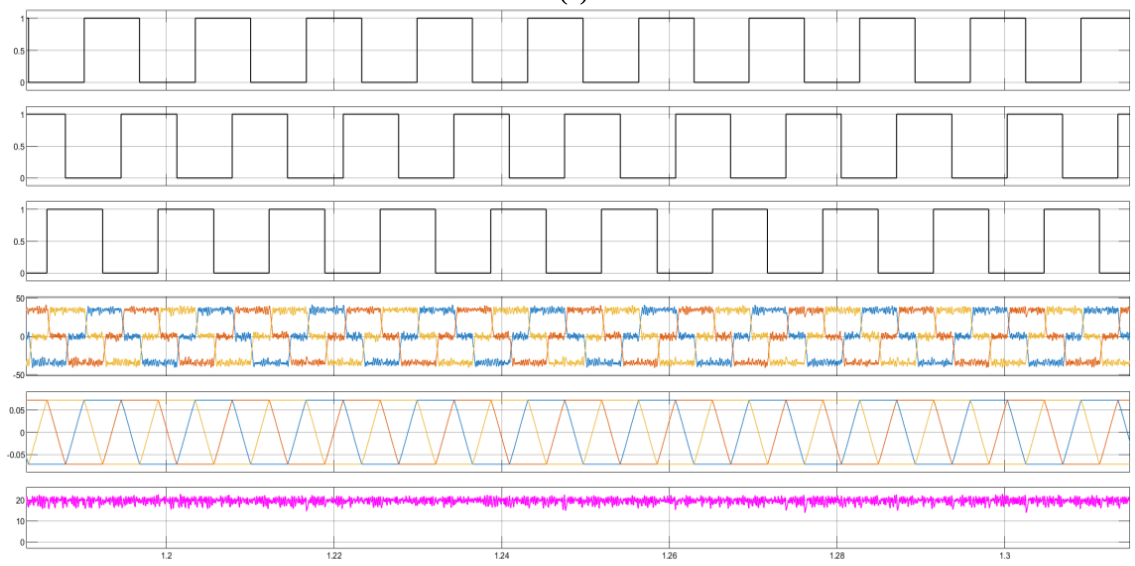

(b)

Figure 8. Decoder circuit waveforms: (a) BSC method and (b) HCC method, where yellow = phase A, blue = phase B, and red = phase C

2.4. Experimental setup

The hardware configuration of the drive system includes several main components such as a DSP–based controller board (TMS320F28379D) and an inverter driver module board that consists of a gate driver, current sensor, and isolated power converter connected to a BLDC motor complete with an encoder, as shown in Figure 9. TMS320F28379D is employed for implementing the control algorithm during blanking time operation. MATLAB simulation, which will be derived in this chapter, needs to be integrated with the DSP, as it contains the required Simulink blocks specially designed for the TMS320F28379D. The laboratory experiment setup will be presented in Figure 10. Subsequent sections provide a comprehensive overview of each hardware component state in Table 4.

Table 4. Hardware specifications of the experimental setup

Component	Specification	Component	Specification
Controller	TI TMS320F28379D DSP LaunchPad	Hall sensor	Built-in Hall sensors with 1000 PPR
Processor clock	200 MHz	PWM frequency	10 kHz, 20 kHz, 40 kHz
BLDC motor	320V, 2.7A, 1800 RPM, 0.5HP	MATLAB version	MATLAB/Simulink R2025
Inverter	Three-phase voltage source inverter	Development software	Code Composer Studio
Current sensor	TMCS1107A4		

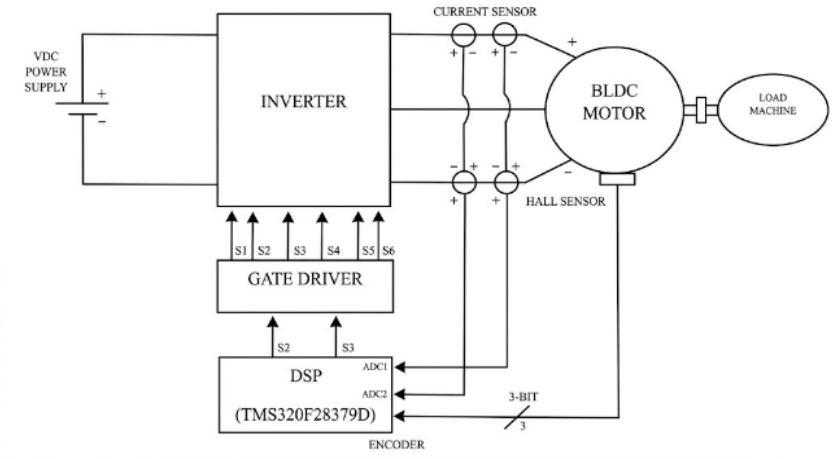

Figure 9. Experimental setup block diagram

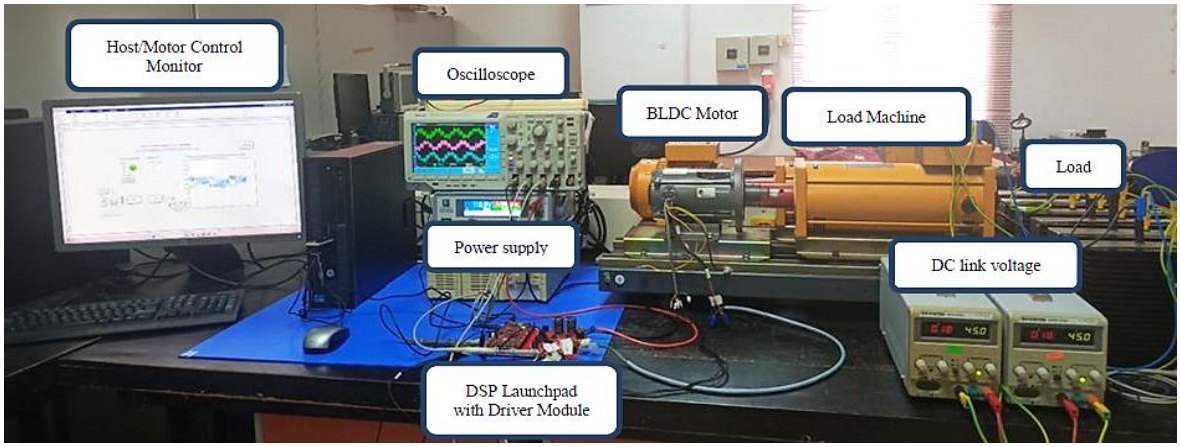

Figure 10. Laboratory experimental setup

2.4.1. Hardware development of hysteresis controller

The internal logic of the hysteresis controller block is the primary decision-making of the system. It processes the error signals for all three motor phases independently to maintain the measured current within a strictly defined tolerance band [21]. The structure of the controller, as shown in the Simulink diagrams in Figure 11(a), consists of three identical parallel channels, which are Phases A, B, and C, and a bandwidth. The implementation of HCC on the TI C2000 F28379D represents a high-performance solution for managing a BLDC motor by integrating precise analog feedback with high-speed digital logic [22]. This simulation model in Figure 11(b) is architected to ensure that the motor's phase currents are maintained within a specific tolerance band, thereby achieving accurate current control through instantaneous switching decisions.

2.4.2. Sensor calibration and zero-offset compensation

In an ideal ADC conversion system, the zero-current reference point is fixed at exactly half the reference voltage (1.65V), corresponding to a digital count of 2048 (for a 12-bit ADC). During the initial hardware testing of the BLDC drive, a systematic bias was observed in Phase B and Phase C, as presented in

Figure 12. With the motor in a stationary state (zero current flow), the ADC recorded a raw value of 2225 for Phase B and 2275 for Phase C in the host file, significantly higher than the theoretical value of 2048.

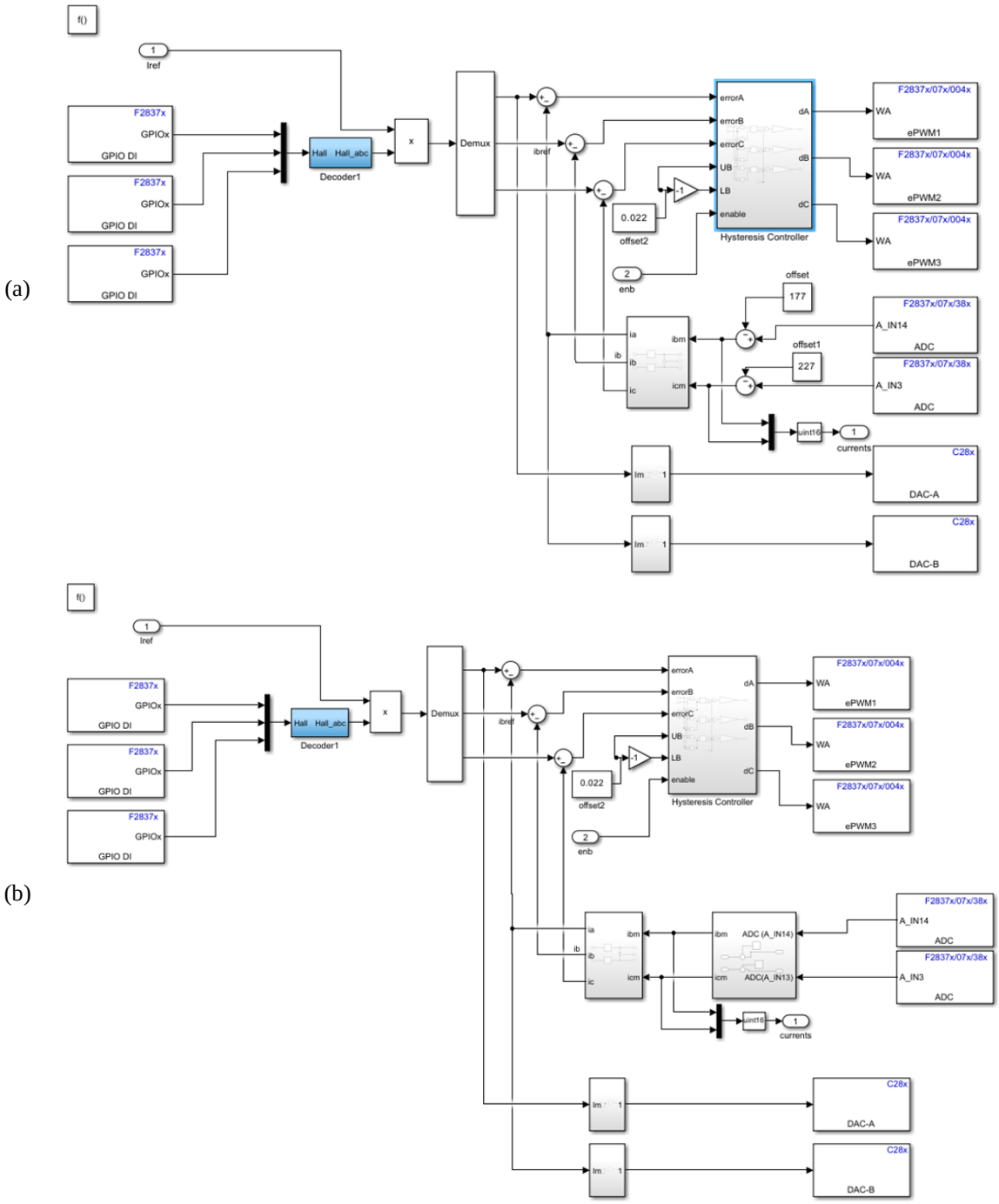

Figure 11. Experimental circuit: (a) hysteresis controller block and (b) current control block

Uncompensated, this positive bias would cause the controller to perceive a non-existent positive current, leading to asymmetric torque generation and inefficient motor control [23], [24]. To rectify this hardware discrepancy, a software-based zero-offset calibration was performed to achieve zero current references, as shown in Figure 13. The necessary correction factor (offset) was calculated by determining the deviation between the measured zero-point and the ideal zero-point using (3).

$$Offset = N_{measured} - N_{\text{ideal}} \quad (3)$$

This offset lifts the zero-ampere point to the exact midpoint of the ADC's measuring range from 0 V to 3.3 V. Consequently, the physical signal is encoded as follows: i) 1.65 V: represents 0 Amps, ii) >1.65 V: represents positive current, and iii) <1.65 V: represents negative current.

Prior to current regulation, a zero-offset calibration procedure was performed to compensate for the inherent offset voltage of the current sensor. During initialization, the motor was maintained at zero current while the sensor output was sampled to determine the offset value. This offset was subsequently subtracted from the measured current during controller operation to improve measurement accuracy and reduce steady-state error. The calibrated current signal was then used as the feedback input for the hysteresis current controller.

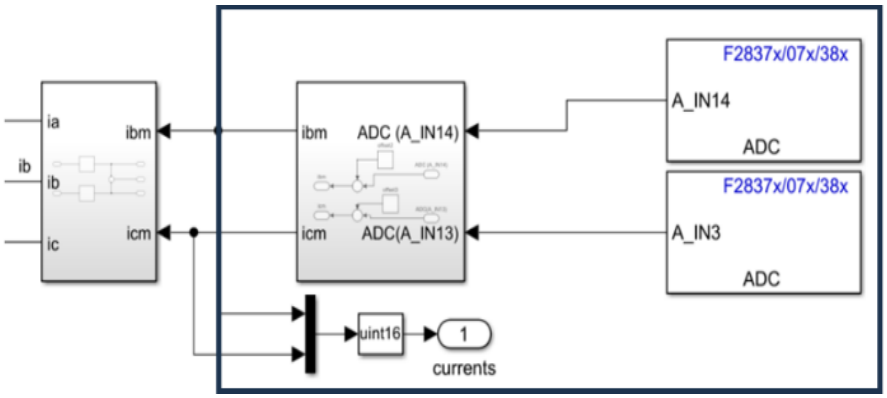

Figure 12. Sensor calibration and zero-offset compensation block

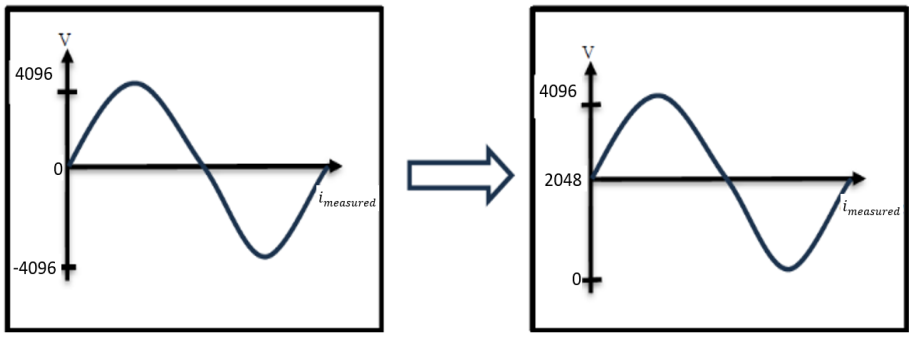

Figure 13. Illustration of zero current references

2.4.3. Selection of hysteresis bandwidth and PWM frequency

The hysteresis bandwidth and PWM frequency were selected to investigate the trade-off between current tracking accuracy and switching performance in the proposed HCC implementation. A narrower hysteresis bandwidth forces the controller to switch more frequently, thereby reducing the current error and improving current tracking performance. However, excessive switching increases switching losses and computational burden. Conversely, a wider hysteresis bandwidth reduces the switching frequency but allows larger current ripple. Therefore, four hysteresis bandwidths (0.022 A, 0.11 A, 0.22 A, and 0.33 A) were selected to represent narrow, medium, and wide operating conditions within the safe operating range of the experimental BLDC drive. Similarly, PWM frequencies of 10 kHz, 20 kHz, and 40 kHz were selected because they represent low, medium, and high switching frequencies commonly adopted in DSP-based BLDC motor drives. These frequencies enable evaluation of the influence of controller sampling capability on current ripple while maintaining reliable real-time execution on the TMS320F28379D DSP platform.

2.4.4. Complete hardware development of MATLAB/Simulink design for HCC main system

Figure 14 shows the main Simulink model deployed on the TMS320F28379D DSP. It contains the real-time control loop, including Hall sensor inputs, current ADC readings, hysteresis comparators, the decoder logic (Boolean expressions), and ePWM modules that directly drive the inverter. This model is

compiled to C code and executed on the DSP [25] at the selected PWM frequency (10–40 kHz). It forms the core of the HCC implementation.

Figure 15 illustrates the host model running on a PC connected to the DSP via serial communication (SCI). It receives real-time data from the target (measured currents, reference values, error signals) and sends commands such as start/stop, speed reference, or hysteresis bandwidth changes. The host model is used for monitoring, data logging, and interactive tuning without recompiling the main controller.

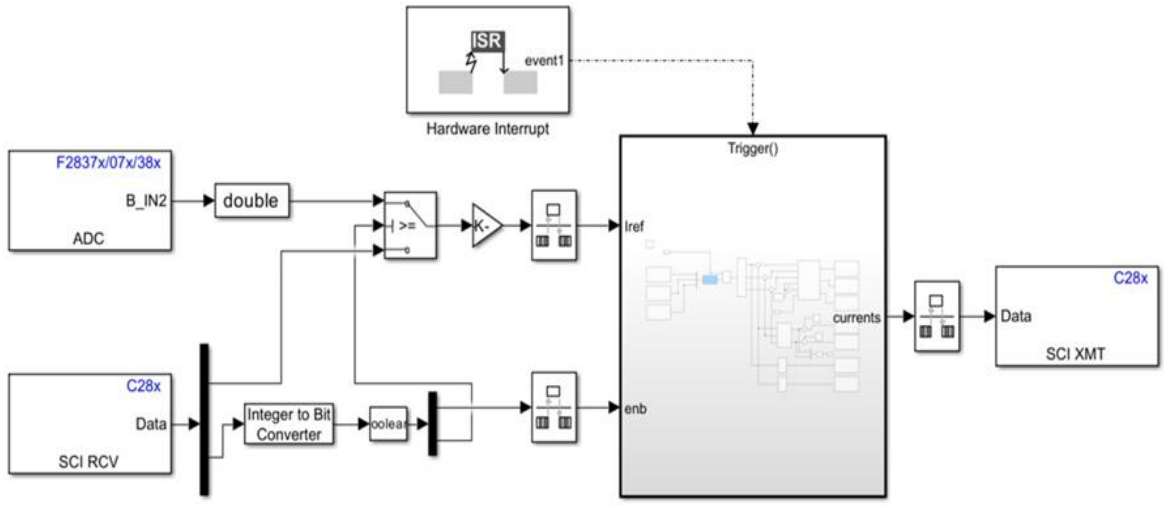

Figure 14. Hardware Simulink design for HCC main system

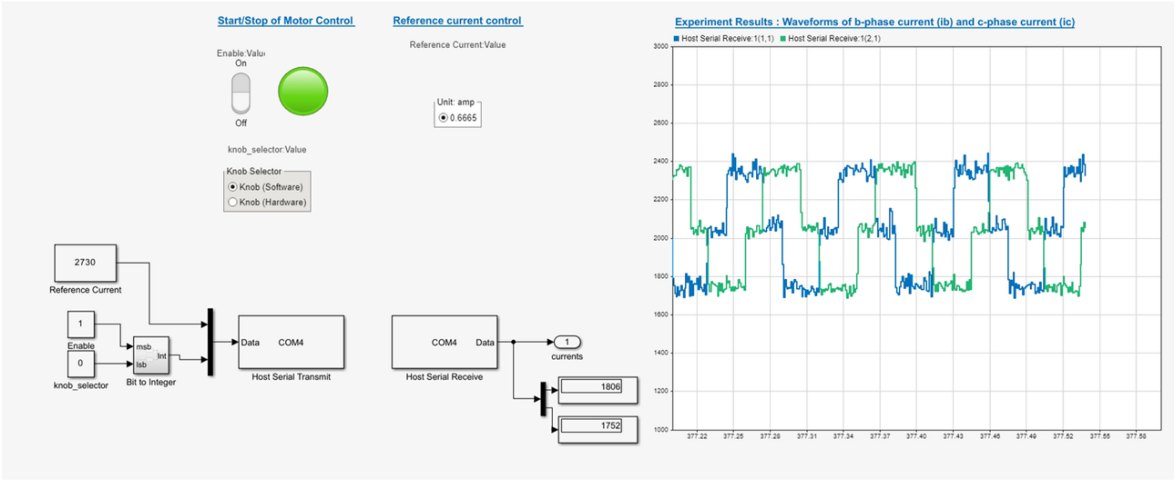

Figure 15. Hardware Simulink design for HCC host system

3. RESULTS AND DISCUSSION

In this section, it explains the results of research from this simulation need to be analyse and compare in terms of the speed, current and torque control performances due to variations of speed and hysteresis bandwidth produced in BSC and HCC conventional of BLDC motor.

3.1. Simulation

Table 5 summarizes the experimental results for the basic switching commutation (BSC) method. The speed response shows a noticeable overshoot and slow settling, while the torque waveform exhibits large low-frequency ripples. The phase current is highly distorted with significant overshoot, leading to a current ripple of approximately 10.12% and a torque ripple of 47.6%. These results confirm that BSC lacks adequate

current regulation, causing poor dynamic performance and increased mechanical vibration. Experimental results for the hysteresis current control (HCC) method under the same operating conditions. The speed response is smooth with no overshoot, and the torque waveform shows only minor high-frequency fluctuations. The phase current is well-regulated, following the reference quasi-square shape, with a current ripple of only 0.52% and a torque ripple of 0.08%. Compared to BSC, HCC reduces current ripple by a factor of nearly 20 and torque ripple by a factor of approximately 600, demonstrating its superior current-regulation capability.

Table 5. Experimental results for BSC and HCC

BSC	HCC
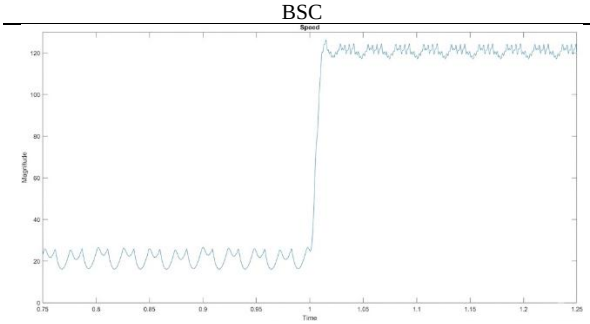	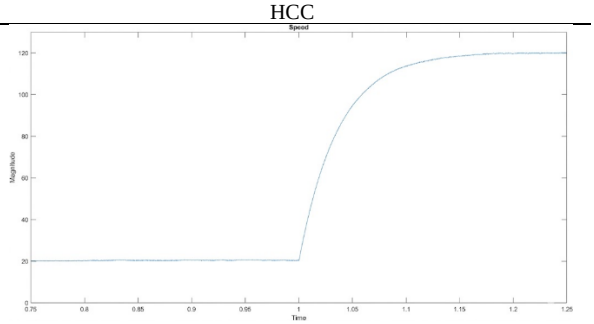
Speed response	Speed response
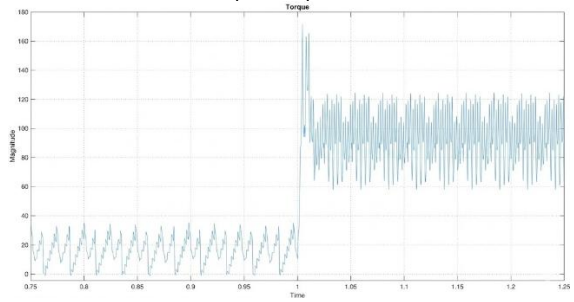	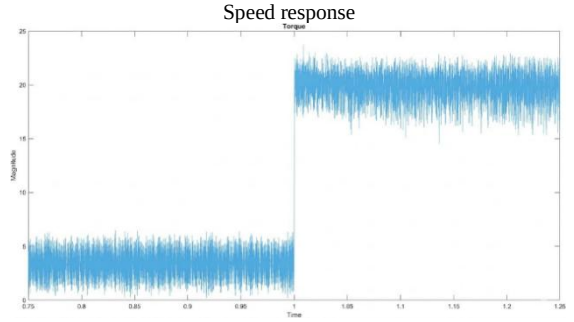
Torque output	Torque output
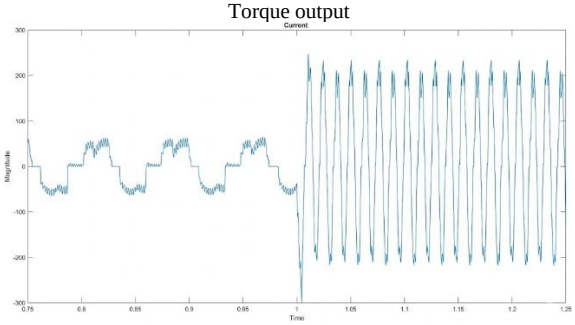	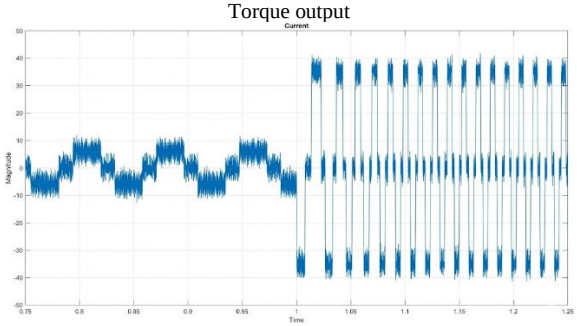
Current behavior	Current behavior

3.2. Effect of hysteresis bandwidth on current ripple

Table 6 shows the effect of hysteresis bandwidth on the measured current ripple at a constant PWM frequency of 40 kHz. The results indicate a clear relationship between hysteresis bandwidth and current tracking performance. When the hysteresis bandwidth is reduced from 0.33 A to 0.022 A, the current ripple decreases from 41.01% to 12.00%. This improvement occurs because a narrower hysteresis band allows the controller to respond to smaller deviations between the reference and measured current, thereby maintaining the phase current closer to its reference value.

However, the reduction in hysteresis bandwidth also increases the switching activity of the inverter. A wider hysteresis band allows a larger current deviation before the switching state is changed, resulting in lower switching activity but higher current ripple. Therefore, the selection of hysteresis bandwidth represents a trade-off between current tracking accuracy and switching stress. The results indicate that the 0.022 A bandwidth provides the lowest measured current ripple among the tested conditions, although the associated increase in switching activity should be considered in practical applications.

Figure 16 illustrates the measured current waveforms of the BLDC motor under different hysteresis bandwidths of 0.022 A, 0.11 A, 0.22 A, and 0.33 A, while maintaining a constant PWM frequency of 40 kHz. The results demonstrate that the hysteresis bandwidth significantly influences current tracking performance

and current ripple. At a bandwidth of 0.022 A, the measured current exhibits the smallest deviation from its reference, resulting in the lowest current ripple. As the hysteresis bandwidth increases to 0.11 A and 0.22 A, the current deviation becomes more noticeable due to the wider allowable current error range. At 0.33 A, the current exhibits the largest variation among the tested conditions, indicating reduced current tracking accuracy. These observations are consistent with the results presented in Table 6, where the current ripple increases from 12.003% at 0.022 A to 24.006% at 0.11 A, 30.0075% at 0.22 A, and 41.0105% at 0.33 A. Therefore, a narrower hysteresis bandwidth provides better current regulation and reduces current ripple, although it may result in increased switching activity.

Table 6. Percentage of current ripple due to various bandwidths

PWM frequency	Hysteresis bandwidth	Percentage of current ripple
40 kHz	0.022 A	12.0030%
	0.11 A	24.0060%
	0.22 A	30.0075%
	0.33 A	41.0105%

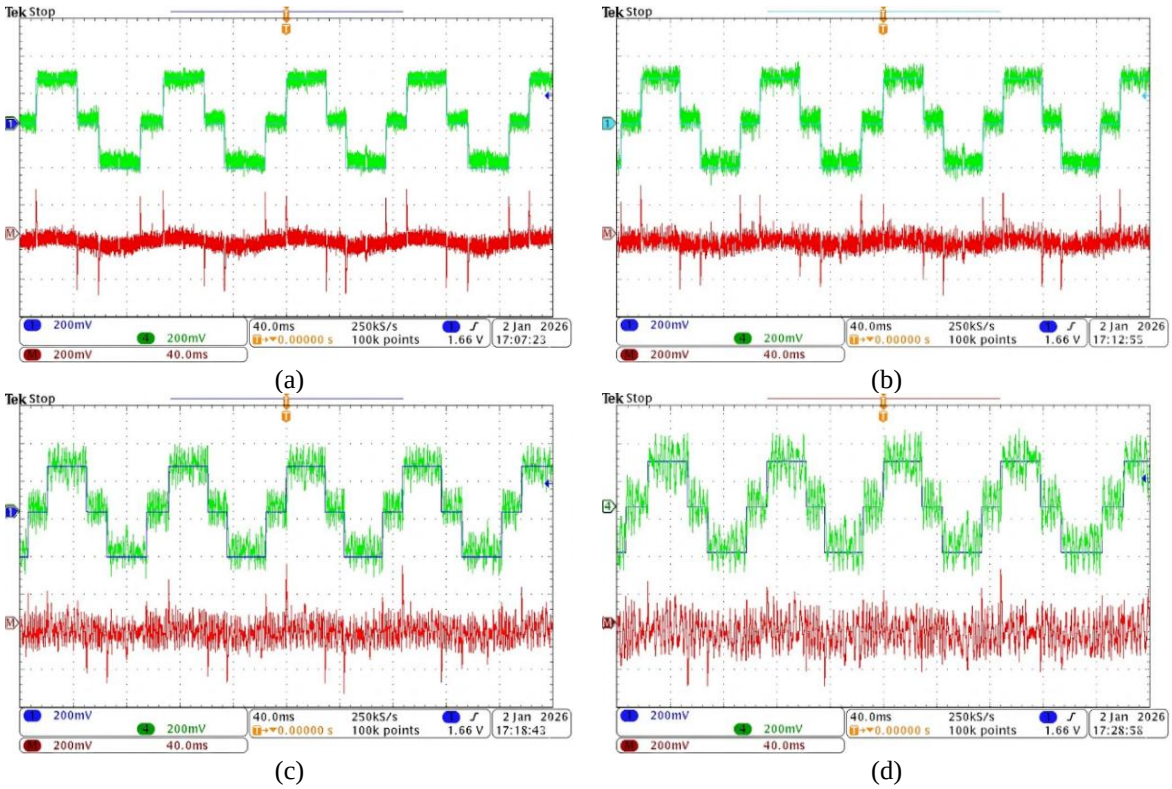

Figure 16. Current waveforms under different hysteresis bandwidths: (a) HCC results at 40 kHz with BW = 0.022; (b) HCC results at 40 kHz with BW = 0.11; (c) HCC results at 40 kHz with BW = 0.22; and (d) HCC results at 40 kHz with BW = 0.033

3.2.1. Performance analysis on current ripple due to different sampling frequencies

Table 7 presents the effect of PWM frequency on current ripple while maintaining a constant hysteresis bandwidth of 0.022 A. Increasing the PWM frequency from 10 kHz to 40 kHz reduces the measured current ripple from 24.01% to 12.00%. At a lower PWM frequency, the controller has a longer sampling interval between switching decisions, allowing a larger deviation of the measured current from the reference before corrective switching occurs. Increasing the PWM frequency provides more frequent current updates and switching decisions, enabling the controller to respond more rapidly to current deviations and maintain closer current tracking.

The results in Table 7 show that the PWM-frequency setting affects the current-regulation performance of the hysteresis controller. The 40 kHz condition provides the lowest current ripple among the tested frequencies. However, increasing the PWM frequency also increases the number of switching events, which may increase switching losses and impose a greater computational requirement on the DSP. Therefore,

the PWM frequency should be selected by considering both current tracking performance and the practical limitations of the power converter and digital controller.

Table 7. Percentage of current ripple due to various PWM frequencies

Hysteresis bandwidth	PWM frequency	Percentage of current ripple
0.022 A	10 kHz	24.0060 %
	20 kHz	18.0045%
	40 kHz	12.0030%

Figure 17 shows the current waveforms under different PWM frequencies of 10 kHz, 20 kHz, and 40 kHz, while maintaining a constant hysteresis bandwidth of 0.022 A. The results indicate that increasing the PWM frequency reduces current ripple and improves current tracking performance. As shown in Table 7, the current ripple decreases from 24.006% at 10 kHz to 18.0045% at 20 kHz and 12.003% at 40 kHz. This improvement is attributed to more frequent switching updates, allowing the controller to respond faster to current deviations and maintain better current regulation.

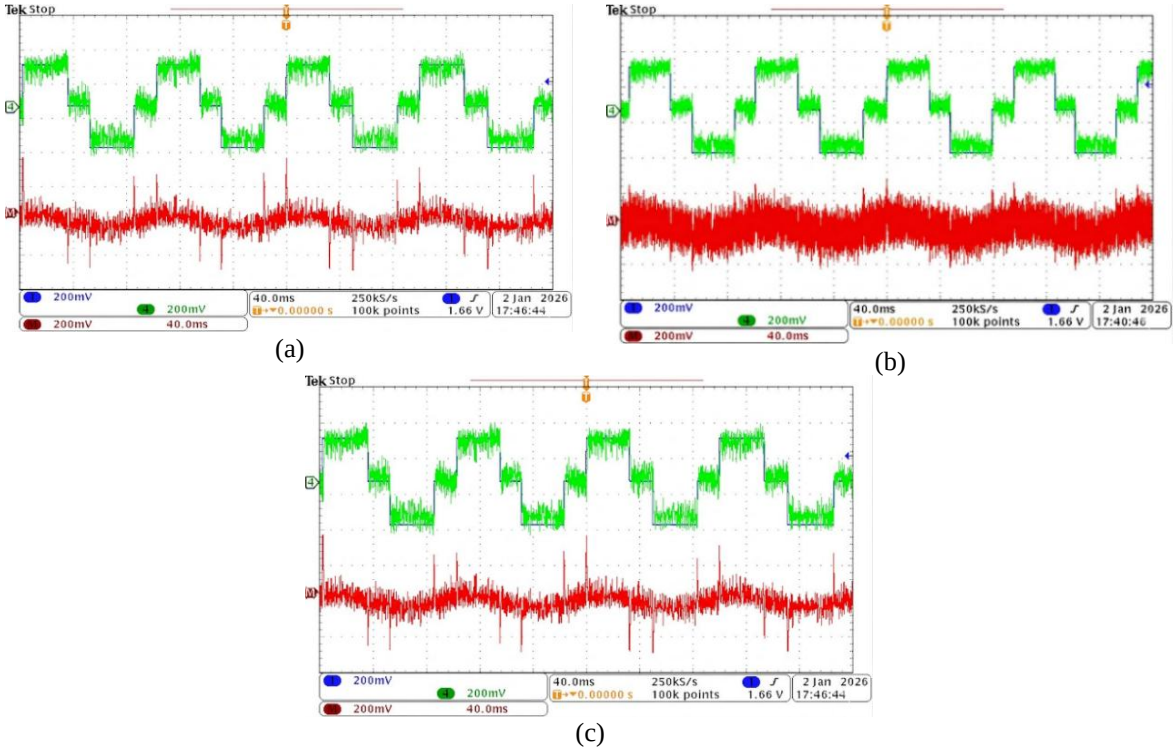

Figure 17. Current waveforms under various PWM frequencies: (a) HCC Results, BW = 0.022 and PWM frequency 10 kHz, (b) HCC results, BW = 0.022 and PWM frequency 20 kHz, and (c) HCC Results, BW = 0.022 and PWM frequency 40 kHz

3.2.2. Three phases of waveform based on ideal conditions

Figure 18 shows the three measured phase currents (i_a, i_b, i_c) together with the reference current (i_{ref}) under ideal HCC conditions: hysteresis bandwidth $HB = 0.022$ A and PWM frequency $f_{\text{PWM}} =$ 40 kHz. The waveforms are balanced and exhibit the expected 120° phase shifts between phases. Due to the narrow hysteresis band and high sampling frequency, each phase current tightly follows its quasi-square reference with minimal ripple (approximately 12%). The narrow band forces the inverter to switch rapidly, keeping the current error within ± 0.022 A, while the high PWM frequency (40 kHz) ensures that the controller detects and corrects errors every 25 µs. As a result, the phase currents are well-regulated and symmetric, producing smooth electromagnetic torque with negligible low-frequency pulsations. These results confirm that the combination of a narrow hysteresis band and high sampling frequency is essential for achieving high-quality current regulation in HCC-controlled BLDC drives.

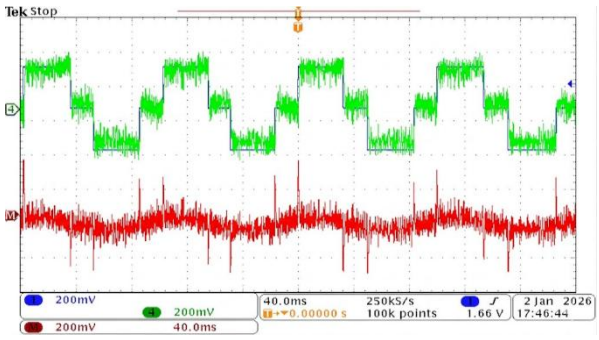

Figure 18. Three phases of current (i_a, i_b, i_c)

4. CONCLUSION

This work developed and implemented a hysteresis current control (HCC) strategy for a three-phase Brushless DC (BLDC) motor using the Texas Instruments TMS320F28379D DSP. The controller was developed in MATLAB/Simulink and successfully deployed to the DSP platform for real-time experimental validation. The proposed implementation integrates Hall sensor decoding, current sensing, and hysteresis current regulation to achieve accurate phase current control in the BLDC motor drive.

The simulation and experimental comparisons indicate that HCC provides improved phase-current regulation over the conventional basic switching commutation (BSC) approach under the conditions examined. The bandwidth tests show that reducing the hysteresis interval lowers the measured current ripple by keeping the actual current closer to its reference. The PWM-frequency tests also show a reduction in ripple as the frequency is increased from 10 kHz to 40 kHz. In the BSC-to-HCC comparison, the reported current-ripple value decreases from 10.12% to 0.52%. The findings therefore demonstrate the importance of selecting suitable hysteresis-bandwidth and PWM-frequency settings when designing the current-regulation function.

Overall, the developed HCC implementation demonstrates a practical and effective current control solution for DSP-based BLDC motor drives, offering improved current quality and stable operation while maintaining a relatively simple control structure suitable for real-time implementation. Further evaluation should consider a wider range of operating speeds and variable load disturbances. Additional work may also quantify electromagnetic torque behavior, torque ripple, and overall drive efficiency to provide a broader assessment of the controller for industrial and electric-vehicle applications.

ACKNOWLEDGEMENT

The authors wish to express their gratitude to the Universiti Teknikal Malaysia Melaka (UTeM), Fakulti Teknologi dan Kejuruteraan Elektrik (FTKE), Centre of Robotic and Industrial Automation (CERIA) and Centre of Research and Innovation Management (CRIM).

FUNDING INFORMATION

Authors state no funding involved.

AUTHOR CONTRIBUTIONS STATEMENT

This journal uses the Contributor Roles Taxonomy (CRediT) to recognize individual author contributions, reduce authorship disputes, and facilitate collaboration.

Name of Author	C	M	So	Va	Fo	I	R	D	O	E	Vi	Su	P	Fu
Amir Haziq Nordin	✓	✓	✓	✓	✓	✓		✓	✓	✓			✓	
Auzani Jidin		✓			✓	✓		✓	✓	✓	✓	✓		
Azrita Alias	✓		✓	✓		✓				✓			✓	✓
Tole Sutikno		✓			✓				✓		✓	✓		

C : **C**onceptualization
M : **M**ethodology
So : **So**ftware
Va : **Va**lidation
Fo : **Fo**rmal analysis
I : **I**nvestigation
R : **R**esources
D : **D**ata Curation
O : Writing - **O**riginal Draft
E : Writing - Review & **E**diting
Vi : **Vi**sualization
Su : **Su**pervision
P : **P**roject administration
Fu : **Fu**nding acquisition

CONFLICT OF INTEREST STATEMENT

Authors state no conflict of interest.

DATA AVAILABILITY

The data that support the findings of this study are available from the corresponding author, [AJ], upon reasonable request.

REFERENCES

[1] M. Şen and M. Mutluer, "A review of BLDC motors: types, application, failure modes and detection," *Energies*, vol. 18, no. 24, Dec. 2025, doi: 10.3390/en18246402.

[2] A. A. Kaplan, M. O. Gulbahce, and D. A. Kocabas, "Sensorless sector determination of brushless DC motors using maximum likelihood estimation," *Machines*, vol. 14, no. 1, Dec. 2025, doi: 10.3390/machines14010042.

[3] D. Joshi, D. Deb, and S. M. Muyeen, "Comprehensive review on electric propulsion system of unmanned aerial vehicles," *Frontiers in Energy Research*, vol. 10, May 2022, doi: 10.3389/fenrg.2022.752012.

[4] A. Gundogan and A. F. Bakan, "Torque ripple reduction in surface-mounted permanent magnet machine with model-based current reference control," *Electronics*, vol. 15, no. 6, Mar. 2026, doi: 10.3390/electronics15061240.

[5] M. A. Khan, H. Ali, and D.-Z. Baig, "Torque ripple mitigation of brushless direct current motors for electric vehicles using novel hybrid control technique of proportional-integral controller and deep reinforcement learning," *Measurement*, vol. 273, May 2026, doi: 10.1016/j.measurement.2026.121139.

[6] N. Prabhu, R. Thirumalaivasan, and B. Ashok, "Critical review on torque ripple sources and mitigation control strategies of BLDC motors in electric vehicle applications," *IEEE Access*, vol. 11, pp. 115699–115739, 2023, doi: 10.1109/ACCESS.2023.3324419.

[7] M. Z. Aihsan, A. Jidin, A. Alias, S. A. Ahmad Tarusan, Z. Md Tahir, and T. Sutikno, "Torque ripple minimization in direct torque control at low-speed operation using alternate switching technique," *International Journal of Power Electronics and Drive Systems (IJPEDS)*, vol. 13, no. 1, pp. 631-642, Mar. 2022, doi: 10.11591/ijpeds.v13.i1.pp631-642.

[8] W. Li, Y. Zhang, and L. Zhu, "An improved rotor position and speed estimation method for PMSM with Hall sensors," *Processes*, vol. 12, no. 10, Oct. 2024, doi: 10.3390/pr12102267.

[9] D. Yu, H. Yi, F. Zhuo, Y. Li, and X. Jiang, "Hysteresis current controller with fixed switching frequency and phase for interleaved converters," *IEEE Transactions on Power Electronics*, vol. 39, no. 12, pp. 15376–15388, 2024, doi: 10.1109/TPEL.2024.3440630.

[10] W. Benjamim, I. Jlassi, and A. J. M. Cardoso, "A computationally efficient model predictive current control of synchronous reluctance motors based on hysteresis comparators," *Electronics*, vol. 11, no. 3, p. 379, Jan. 2022, doi: 10.3390/electronics11030379.

[11] G. Gupta and M. Sreejeth, "Comparative analysis of speed control of BLDC motor using PWM and current control techniques," in *2022 IEEE IAS Global Conference on Emerging Technologies (GlobConET)*, IEEE, May 2022, pp. 610–614, doi: 10.1109/GlobConET53749.2022.9872173.

[12] A. Koduah, G. Svinkunas, A. Bandza, and S. Osei Fobi, "Investigations into higher-frequency hysteresis current controller for supraharmonic hybrid active filters," *Applied Sciences*, vol. 14, no. 5, Feb. 2024, doi: 10.3390/app14051713.

[13] A. I. Abouseda, R. Doruk, A. Emin, and O. Akdeniz, "Modeling, dynamic characterization, and performance analysis of a 2.2 kW BLDC motor under fixed load torque levels and variable speed inputs: an experimental study," *Actuators*, vol. 14, no. 8, Aug. 2025, doi: 10.3390/act14080400.

[14] S. Qiu, D. Makihara, and K. Kiyota, "Torque ripple suppression and current regulation for vector controlled switched reluctance motors," in *2022 IEEE Energy Conversion Congress and Exposition (ECCE)*, IEEE, Oct. 2022, pp. 1–7, doi: 10.1109/ECCE50734.2022.9947865.

[15] K. Sreeram, P. K. Preetha, J. Rodríguez-García, and C. Álvarez-Bel, "A comprehensive review of torque and speed control strategies for switched reluctance motor drives," *CES Transactions on Electrical Machines and Systems*, vol. 9, no. 1, pp. 46–75, Mar. 2025, doi: 10.30941/CESTEMS.2025.00006.

[16] S. Qiu, M. R. Fabio, R. Kokubu, C. Lyu, and K. Kiyota, "Robust current regulation for harmonic current injected torque ripple suppression in switched reluctance motor drives," *IEEE Open Journal of Industry Applications*, vol. 7, pp. 90–103, 2026, doi: 10.1109/OJIA.2025.3649093.

[17] J. C. Gamazo-Real, E. Vázquez-Sánchez, and J. Gómez-Gil, "Position and speed control of brushless DC motors using sensorless techniques and application trends," *Sensors*, vol. 10, no. 7, pp. 6901–6947, Jul. 2010, doi: 10.3390/s100706901.

[18] S. Usha, P. Geetha, A. Geetha, R. Palanisamy, and S. Choudhury, "Enhanced battery charging efficiency using torque hysteresis controlled BLDC motor drive for electric vehicle," *Energy Storage and Saving*, vol. 4, no. 4, pp. 373–391, Dec. 2025, doi: 10.1016/j.enss.2025.05.006.

[19] R. M. Sholihah, F. Fahrul, A. Kurniawan, and I. Mahmudi, "Implementation of modified trapezoidal commutation scheme for speed control of 1 kW BLDC motor," *Journal of Mechatronics, Electrical Power, and Vehicular Technology*, vol. 14, no. 2, pp. 127–137, Dec. 2023, doi: 10.14203/j.mev.2023.v14.127-137.

[20] A. Kumar, M. V. Naik, R. Kumar, and Aman, "Design and analysis of BLDC motor speed control for electric vehicles powered by solar PV and grid supply," *Discover Electronics*, vol. 2, no. 1, Jul. 2025, doi: 10.1007/s44291-025-00097-4.

[21] A. Tilli and A. Tonielli, "Sequential design of hysteresis current controller for three-phase inverter," *IEEE Transactions on Industrial Electronics*, vol. 45, no. 5, pp. 771–781, 1998, doi: 10.1109/41.720334.

[22] M. A. Rahman, A. A. Abushaiba, and A. M. Elrajoubi, "Integration of C2000 microcontrollers with MATLAB Simulink Embedded coder: a real-time control application," in *2024 7th International Conference on Electrical Engineering and Green Energy (CEEGE)*, IEEE, Jun. 2024, pp. 131–136, doi: 10.1109/CEEGE62093.2024.10744177.

[23] A. A. Tabassum, H. M. Cho, and M. I. Mahmud, "Essential features and torque minimization techniques for brushless direct current motor controllers in electric vehicles," *Energies*, vol. 17, no. 18, Sep. 2024, doi: 10.3390/en17184562.

[24] M. Nasir, M. Saloumi, and A. B. Nassif, "Review of various metaheuristics techniques for tuning parameters of PID/FOPID controllers," *ITM Web of Conferences*, vol. 43, Mar. 2022, doi: 10.1051/itmconf/20224301002.

[25] A. Entezari, A. D. Kolagar, and M. R. A. Pahlavani, "Real-time implementation of finite control set model predictive control for BLDC Motors with dynamic speed references on ESP32," *IET Power Electronics*, vol. 19, no. 1, Jan. 2026, doi: 10.1049/pel2.70171.

BIOGRAPHIES OF AUTHORS



Amir Haziq bin Nordin was born in Malaysia in 2001. He received his bachelor's degree in electrical engineering from Universiti Teknikal Malaysia Melaka (UTeM), Malaysia, in 2026. He is currently pursuing a Master of Engineering (M.Eng.) degree, also at UTeM. His research interests include motor modelling, control systems, power electronics, electric drive systems, and simulation studies. He can be contacted at email: amirhaziq015@gmail.com.



Auzani bin Jidin received the B.Eng., M.Eng., and Ph.D. degrees in power electronics and drives from Universiti Teknologi Malaysia (UTM), Johor Bahru, Malaysia, in 2002, 2004, and 2011, respectively. He is currently a senior lecturer at the Faculty of Electrical Technology and Engineering, Universiti Teknikal Malaysia Melaka (UTeM), Malaysia. He is also an active researcher with the EV-Prodrives Research Group, focusing on power electronics and drives (PED), electric machine design (EMD), and electric vehicle drives (EVD). His research interests include power electronics, electric motor drive systems, field-programmable gate arrays (FPGAs), digital signal processors (DSPs), and electric vehicle drive technologies. He can be contacted at email: auzani@utem.edu.my.



Azrita binti Alias received the B.Eng. (Hons.) degree in electrical engineering (control and instrumentation) and the M.Eng. degree in electrical engineering from Universiti Teknologi Malaysia (UTM) in 2000 and 2003, respectively, and the Ph.D. degree from the University of Malaya in 2015. She is currently a senior lecturer at the Faculty of Electrical Technology and Engineering, Universiti Teknikal Malaysia Melaka (UTeM), Malaysia. She is also an active researcher with the EV-Prodrives Research Group and serves as the head of the Bachelor of Electrical Engineering with Honours (Part-Time) (BELG) programme at UTeM. Her research interests include modelling, control systems analysis, power electronics, motor drive systems, and engineering applications. She can be contacted at email: azrita@utem.edu.my.



Prof. Ir. Tole Sutikno, S.T., M.T., Ph.D., MIET, IPM., ASEAN Eng., is a lecturer and the head of the Master Program of Electrical Engineering at the Faculty of Industrial Technology, Universitas Ahmad Dahlan (UAD) in Yogyakarta, Indonesia. In addition to leading the Master Program, he also lectures in the Ph.D. Program in Informatics and the Undergraduate Program in Electrical Engineering at UAD. He received his Bachelor of Engineering from Universitas Diponegoro in 1999, Master of Engineering from Universitas Gadjah Mada in 2004, and Doctor of Philosophy in Electrical Engineering from Universiti Teknologi Malaysia in 2016. All three degrees are in the Electrical Engineering area. He has been a Professor at UAD in Yogyakarta, Indonesia, since July 2023, following his tenure as an associate professor in June 2008. He is the Editor-in-Chief of TELKOMNIKA and Head of the Embedded Systems and Power Electronics Research Group (ESPERG). He is listed as one of the top 2% of researchers worldwide, according to Stanford University and Elsevier BV's list of the most influential scientists from 2021 to the presents. His research interests cover digital design, industrial applications, industrial electronics, industrial informatics, power electronics, motor drives, renewable energy, FPGA applications, embedded systems, artificial intelligence, intelligent control, digital libraries, and information technology. He can be contacted at email: tole@te.uad.ac.id or thsutikno@ieee.org.